

Intra-hour forecasting with a total sky imager at the UC San Diego solar energy testbed

Chi Wai Chow¹, Bryan Urquhart¹, Matthew Lave¹, Anthony Dominguez¹, Jan Kleissl¹, Janet Shields², Byron Washom³

¹Department of Mechanical and Aerospace Engineering

²Marine Physical Laboratory, Scripps Institution of Oceanography

³Director, Strategic Energy Initiatives

University of California, San Diego

Phone: +1 858 534 8087

email: jkleissl@ucsd.edu

Abstract

A method for intra-hour, sub-kilometer cloud forecasting and irradiance nowcasting using a ground-based sky imager at the University of California, San Diego is presented. Sky images taken every 30 seconds were processed to determine sky cover using a clear sky library and sunshine parameter. From a two-dimensional cloud map generated from coordinate-transformed sky cover, cloud shadows at the surface were estimated. Limited validation on four partly cloudy days showed that (binary) cloud conditions were correctly nowcast 70% of the time for a network of six pyranometer ground stations spread out over an area of 2 km². Cloud motion vectors were generated by cross-correlating two consecutive sky images. Cloud locations up to five minutes ahead were forecasted by advection of the two-dimensional cloud map. Cloud forecast error increased with increasing forecast horizon due to high cloud cover variability over the coastal site.

1. Introduction

Integration of large amounts of photovoltaics (PV) into the electricity grid poses technical challenges due to the variable nature of the solar resource. The ability to forecast solar irradiation will allow grid operators to better accommodate the variable electricity generation in their scheduling, dispatching, and regulation of power. Currently, physically based forecasting is primarily conducted using numerical weather prediction (NWP) and satellite cloud observations. NWP provides information up to several days ahead, however there are significant biases and random errors in the irradiance estimates (Remund et al. 2008, Lorenz et al. 2009, Perez et al. 2010, Mathiesen and Kleissl 2011). The spatial resolution of NWP is coarse at about 100 km^2 , but there is active research on high-resolution rapid refresh models with grid cell areas of less than 10 km^2 (Benjamin et al. 2010, Lara-Fanego et al. 2011). Either way, most clouds will remain unresolved in NWP. Frozen cloud advection based on GOES satellites images can provide accurate forecasts up to six hours ahead (Perez et al. 2010, Schroedter-Homscheidt 2009) at a resolution of 1 km^2 .

To achieve high temporal and spatial resolution for intra-hour forecasts, NWP and Satellite forecasts are currently inadequate. Ground observations using a sky imager present an opportunity to fill this forecasting gap and deliver a sub-kilometer view of cloud shadows over a central PV power plant or an urban distribution feeder.

The advanced smart 42 MW_P microgrid of the University of California, San Diego (UCSD) is one of the world's most densely monitored environments with over 18,000 measurement points per km^2 , including a hemispherical sky imager (Fig. 1). The UCSD microgrid provides a globally unique testbed for a customer side of the meter smartgrid with renewable generation, thermal, and electricity energy storage, demand side management, and demand response. In this paper, we demonstrate how intra-hour cloud shadows are forecasted and irradiance is nowcasted for the UCSD microgrid. In Section 2, we describe our experimental setup, present methods to obtain sky cover, cloud motion, irradiance, and to forecast cloud locations and irradiance. Existing literature on sky imaging systems and image processing is also reviewed in Section 2. In Section 3, we present the results for cloud shadow

1 mapping onto ground stations as nowcasting and cloud forecasting using sky imagery. Conclusions
2 are presented in Section 4.

3 Nomenclature

| | | | |
|------------------|---|-------------|--|
| alt | altitude [m] | $lat(0)$ | latitude of TSI [°] |
| am | relative optical airmass | $lat(i, j)$ | latitude of location i, j [°] |
| dt | forecast horizon [sec] | $lon(0)$ | longitude of TSI [°] |
| e_m | matching error | $lon(i, j)$ | longitude of location i, j [°] |
| $e_{m,p}$ | matching error assuming cloud persistence | P_{false} | Number of false pixels |
| e_{cap} | cloud-advection-versus-persistence error | P_{total} | Number of total pixels |
| f_{h1} | $\exp(-alt/8000)$ | r_{lat} | resolution of the ground latitude grid [°] |
| f_{h2} | $\exp(-alt/1250)$ | r_{lon} | resolution of the ground longitude grid [°] |
| GHI | global horizontal irradiance [$W\ m^{-2}$] | T_L | Linke Turbidity coefficient |
| GHI_{csk} | clear sky global horizontal irradiance [$W\ m^{-2}$] | x | distance in eastern direction, positive eastward [m] |
| ΔH | cloud base height above ground level at TSI location [m] | $x_p(i, j)$ | column pixel coordinate in cloud map of solar vector intersection at height ΔH |
| $\Delta H(i, j)$ | cloud base height above ground level at location i, j [m] | y | distance in northern direction, positive northward [m] |
| I_o | solar constant, $1366.1\ [W\ m^{-2}]$ modulated by the inverse square of the earth-sun distance | $y_p(i, j)$ | row pixel coordinate in cloud map of solar vector intersection at height ΔH |
| i, j | indexed location on ground grid corresponding to a particular latitude, longitude and altitude | θ | solar zenith angle [°] |
| kt | Clear sky index, GHI/GHI_{csk} | ϕ | solar azimuth angle [°] |
| ℓ_{lat} | length of a unit latitude at the TSI latitude [m] | θ_p | pixel zenith angle [°] |
| ℓ_{lon} | length of a unit longitude at the TSI longitude [m] | ϕ_p | pixel azimuth angle [°] |

4 2. Methods

5 2.1 Experimental Setup

6 A rooftop mounted TSI 440A total sky imager (TSI, Yankee Environmental Systems , setup at
7 $32.8852^\circ N$, $117.2400^\circ W$, 124 m MSL) has taken images of the sky over UCSD since August 2009 (Fig.
8 2). The instrument consists of a spherical mirror and a downward pointing camera. Images are taken
9 every 30 seconds when the sun is above an elevation angle of three degrees. The camera provides
10 images that are 640 by 480 pixels and the mirror occupies 420 by 420 pixels.



Figure 1: Map of UCSD showing sky imager coverage, weather stations, and PV arrays. The coverage area of the sky imager is a function of cloud base height. The region displayed here has a radius of approximately 2 kilometers which would apply to a cloud base height of 1150 m at a maximum zenith angle of 65°. © Google Maps, 2010



Figure 2: TSI 440A Total Sky Imager.

The image output settings by the TSI data acquisition software are default and cannot be changed. Images are 24-bit compressed jpgs. The compression process induces a small loss of information in the image. Additionally the system has an automatic gain adjustment to provide a larger dynamic range for the 8 bits on each of the red, green and blue channels. This adjustment process causes the intensity histogram of each channel to redistribute and thus the relative spectral composition of the images to fluctuate slightly with incoming signal strength. To determine sky cover obstructed by the camera arm and the shadowband, image masks are generated, edges of the masks are identified, and pixel values of the edge region are used to interpolate the region within.

2.2 Cloud Decision Algorithm

Sky imagers provide a visual measurement of a whole sky dome with high temporal and spatial resolution. Spatial resolution is determined by the camera's ability to resolve a single picture element (pixel), the solid angle subtended by this pixel, and the distance of the cloud from the imager which is a function of its cloud base height (CBH) and zenith angle (ZA). Temporal resolution is dictated primarily by the operational ability of the image processing algorithm. Atmospheric properties such as aerosol

optical depth, cloud optical depth, cloud cover, cloud type, and CBH have been retrieved using sky imagers developed by research groups (Cazorla et al. 2008, 2009, Heinle et al. 2010, Kassianov et al. 2005, Long et al. 2006, Huo and Lu 2009, 2010, Kalisch and Macke, 2008, Pfister et al. 2003, Seiz et al. 2007, Shields et al, 2007, 2009). Typical components of a sky imager are a charge coupled device (CCD) camera, a fisheye lens, an environmental housing, and possibly a solar occulter depending on the choice of CCD sensor and application.

The TSI data acquisition software provides a cloud decision output image, however, we developed our own algorithm and all images processing are done on raw image output. Our cloud detection technique is based on the concept of the ratio of the red channel to the blue channel developed at the Scripps Institution of Oceanography (Johnson et al. 1989, 1991, Shields et al., 2007, 2009). Increased molecular (Rayleigh) scattering of shorter wavelengths causes the clear sky to be blue and the signal measured in the blue channel to be larger. Since clouds scatter the visible wavelengths more evenly, the red signal is similar to the blue signal. The red-blue-ratio (RBR) indicates whether the dominant source of the scattered light incident on a pixel is the clear sky or a cloud.

The RBR in the whole sky hemisphere in clear conditions is not uniform due to aerosol and airmass effects. Due to the size distribution of aerosols relative to the wavelength of incident visible light, scattering by aerosols shows a weaker wavelength dependence than scattering by molecules (McCartney 1976), which results in the scattered light appearing white. This is apparent near the horizon where relative optical airmass increases and more total aerosols occupy the optical path through the atmosphere. In the circumsolar region the forward scattering effects of aerosols are also apparent as a white region around the sun. Because of these effects, a single RBR threshold for the entire image is not appropriate. Rather a clear sky library (CSL based on Shields et al., 2009) as a function of zenith and sun-pixel-angle was calculated from images on a cloud-free day (section 3.2). A clear sky background image is then generated for each sky image based on the current solar ZA (Fig. 3b). A pixel is classified as cloudy if its RBR (Fig. 3c) is larger than the RBR in the clear sky background image by more than a threshold value. The RBR of clouds is usually larger than the blue

1 sky. Outside the circumsolar region (small sun-pixel-angles), the method using the threshold from CSL
 2 is able to detect clouds accurately. However, within the circumsolar region, thick opaque clouds appear
 3 darker, have a lower RBR than the clear sky, and cannot be detected using the CSL. A sunshine
 4 parameter (SP, defined by Pfister et al. 2003) is used in addition to the CSL to improve cloud decision
 5 in the circumsolar region. SP is computed as the average RBR of the pixel area on the shadowband
 6 around the sun position (indicated in Fig. 3a). SP is a dynamic single-valued RBR threshold that
 7 changes from image to image, and is typically small when the sun is obscured. Pixels with $RBR > SP$
 8 are classified as cloudy even if the CSL indicates otherwise. By adding the clouds detected using the
 9 CSL (Fig. 3e) to the clouds detected using SP (Fig. 3d), the overall cloud decision image is obtained
 10 (Fig. 3f).

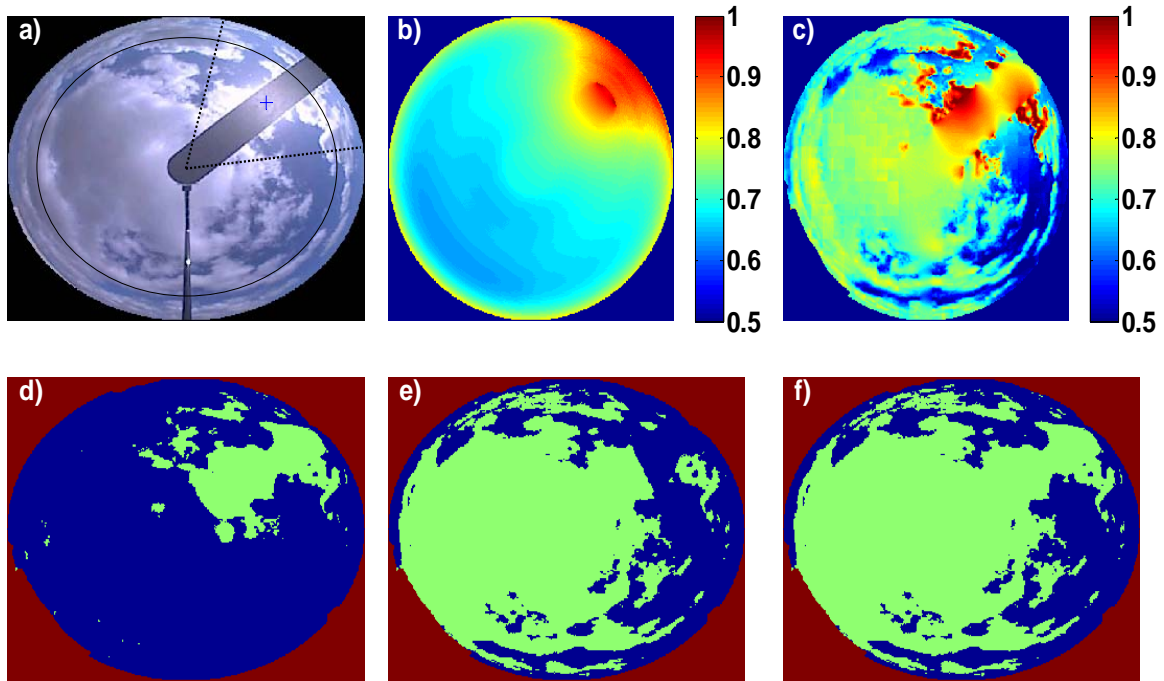


Figure 3: Processing chain of a sky image on October 4, 2009 15:45:30 PST (a) to obtain the cloud decision image. The sunshine parameter is 0.85 and is evaluated around the sun position indicated by the blue cross. The dotted black lines show the borders of the circumsolar region defined as solar azimuth $\pm 35^\circ$ and the solid black line shows ZA at 65° . (b) Clear sky RBR (colorbar) background image plus the threshold. (c) RBR (colorbar) image. (d) Pixels in (c) with $RBR > SP$ or (e) $RBR > CSL$ are assumed to be cloudy. (f) Shows the final cloud decision image. Green areas are clouds and blue areas are clear skies

Once a cloud decision image has been generated, the cloud fraction is computed as the number of cloudy pixels divided by the total number of sky pixels with the solid angle correction described by Long et al. (2006). The cloud decision image is transformed to sky coordinates to geolocate clouds for cloud shadow mapping and forecasting using a geometric transformation that assumes constant CBH throughout the image

$$\begin{Bmatrix} x \\ y \end{Bmatrix} = \Delta H \tan \theta_p \begin{Bmatrix} \sin \phi_p \\ \cos \phi_p \end{Bmatrix}. \quad (1)$$

The CBHs were obtained from a ceilometer at Miramar Naval Air Station (KNKX, 32.8759°N, 117.1366°W, 141 m MSL, 9.5 km east of the TSI) since the imagery was taken before a ceilometer was installed at the site. The sky coordinate image (hereinafter cloud map) is restricted to ZAs less than 65° since the coordinate transformation near the horizon is not valid (Beaubien and Freedman 2001).

2.3 Irradiance Estimation

Prior techniques for estimating global horizontal irradiance (GHI) over an extended area consisted of satellite-derived cloud cover coupled with an empirical clear sky model (Cano et al. 1986, Schmetz 1989, Zelenka et al. 1999, Perez et al. 2002, Rigollier et al. 2004, Pereira et al. 2000, Martins et al. 2007). On the other hand, ground based instruments are typically point sensors and do not provide spatial irradiance information.

The primary factor modulating GHI from its clear sky value is the presence of a cloud between the ground location and the sun as this directly attenuates the solar beam irradiance. Variations in diffuse irradiance caused by changing cloud distribution and optical depth are smaller and generally negatively correlated with beam irradiance (a possible exception is cloud enhancement effects which are beyond the scope of this paper, Luoma et al. 2011). To estimate the sky conditions between a given ground point and the sun, the intersection of the vector to the sun from that point on the ground to the cloud map is computed. The ground around the TSI is gridded (hereinafter ground map) into 10 x 10 m cells

1 extending 5 km in each of the four cardinal directions. The pixel coordinate of the intersection of the
 2 solar vector with the cloud map for the (i, j) element of the ground map is:

$$x_p(i, j) = \frac{\tan \theta \sin \phi}{\ell_{lon} r_{lon}} \Delta H(i, j) + \frac{\text{lon}(i, j) - \text{lon}(0)}{r_{lon}}, \quad (2)$$

$$y_p(i, j) = -\frac{\tan \theta \cos \phi}{\ell_{lat} r_{lat}} \Delta H(i, j) + \frac{\text{lat}(i, j) - \text{lat}(0)}{r_{lat}}. \quad (3)$$

3

4 Actual spatial coverage of the GHI estimates within the 100 km² region considered varies with the sun's
 5 position, cloud height and topography, e.g. when the clouds are low, the horizontal component of the
 6 distance to the cloud is smaller and thus the coverage is smaller.

7 To parameterize GHI, the Ineichen clear sky model (Ineichen 2002) as modified by Perez et. al.
 8 (2002) is used :

$$GHI_{csk} = a_1 I_o \cos \theta \exp \left(-a_2 m (f_{h1} + f_{h2}(T_L - 1)) \right) \exp(0.01 a m^{1.8}), \quad (4)$$

$$a_1 = 5.09 \cdot 10^{-5} alt + 0.868 ,$$

$$a_2 = 3.92 \cdot 10^{-5} alt + 0.0387 .$$

9 This model requires the Linke turbidity factor (Linke 1922) as input and has a reported mean bias error
 10 of -6 W m⁻², and a root mean square error of 19 W m⁻² (Ineichen 2006). When the sun is occluded the
 11 GHI is assumed to equal 40% of the clear sky value. This value is chosen because the clouds that
 12 occurred on the days selected for validation were optically thick and reduced the irradiance to
 13 approximately this level. While the computed irradiance is not used in a quantitative evaluation, it is
 14 useful for a qualitative evaluation of the method as presented in section 3.4.

15

16 **2.4 Cloud Motion**

17 Cloud velocity and direction of motion is determined through the cross-correlation method (CCM)
 18 applied to two consecutive sky images (Hamill & Nehrkorn 1993). Before applying the CCM, images

are projected into sky coordinates to remove geometric distortion. The projected sky image is partitioned into subsets of pixels of equal size such that each subset is about 1% of the sky image area. The CCM finds the position that best matches each given subset of pixels in the previous sky image within the current image (Fig. 4). The CCM yields the wind vector (direction and speed) with the largest cross-correlation coefficient (CCC) that specifies the quality of the match. Since the CCM is computationally expensive, the search area is limited to a search distance that is five times the size of the original subset. This search distance effectively sets the largest detectable cloud speed. In general, the CCM obtains a larger correlation coefficient on an area with a high contrast of pixel values, such as a cloud with a sharp boundary in a clear sky. The CCM is performed on the red channel image which has a higher contrast between clear sky and cloud than the blue and green channels (the cloud decision image would have even higher contrast because it is a binary image but no texture information). Future work will use the RBR image because this has higher contrast than the red image.

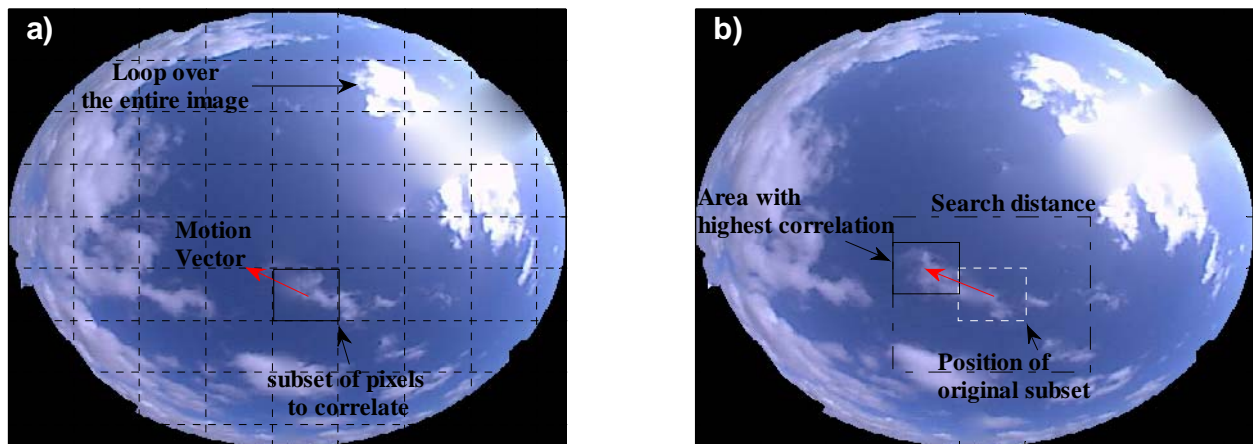


Figure 4: Illustration of the cross-correlation method using two images on October 4, 2009 at 16:18:30 (a) and 16:19:00 PST (b). Each region of pixels from (a) is correlated to (b) within a search distance. The location of the highest correlation is found and a motion vector is defined for each box. The cloud velocity determined from this pair of images was 5.2 m s^{-1} . While the method is illustrated here on a full color sky image, the method is actually applied to the coordinate transformed (Eq. 1) red channel image.

Assuming spatial homogeneity of cloud velocity, the vector field obtained through the CCM is further processed using several quality controls to yield an average cloud velocity across the image.

The circumsolar region is often offscale bright (when a pixel registers the highest possible 8-bit value) and shows little variation over time in clear conditions. This results in erroneously small motion vectors and hence vectors in this region are removed. Using the information in the cloud decision image the CCM is performed only on areas that contain clouds. Only motion vectors with CCC higher than 0.8 are considered. Finally, vectors that are more than one standard deviation from the mean in either the x or y component of the velocity are eliminated. The remaining vectors are vector-averaged to yield the advection velocity of the cloud field. We note that this method needs further development for the case of several cloud layers with different velocity vectors.

2.5 Cloud Forecasting

To forecast cloud cover, the cloud map at time t_o is advected at the speed and direction of the global vector determined from cross-correlating the images at time t_o and $t_o - dt$ ($dt = 30$ seconds). To determine accuracy, the actual cloud map at time $t_o + dt$ (Fig. 5b) is overlaid onto the advected cloud map (Fig. 5c) to determine the pixel-by-pixel forecast error (Fig. 5d). Since the circumsolar region has a large potential for erroneous cloud decision, the sky image is divided into the circumsolar region (within 35° of the solar azimuth angle) and the outer region (Fig. 3a). The matching error between the two cloud maps is

$$e_m = \frac{P_{false}}{P_{total}} \times 100\%, \quad (5)$$

which is the ratio between the number of falsely forecasted pixels and the number of total pixels in a region. The cloud-advection-versus-persistence (cap) error:

$$e_{cap} = \frac{e_m}{e_{m,p}} \times 100\% \quad (6)$$

describes the forecast error obtained by cloud advection (Fig. 5d) divided by the error obtained if the image at t_o was assumed to persist until $t_o + dt$ (no advection). An $e_{cap} < 1$ implies that the cloud advection improves the forecast compared to persistence.

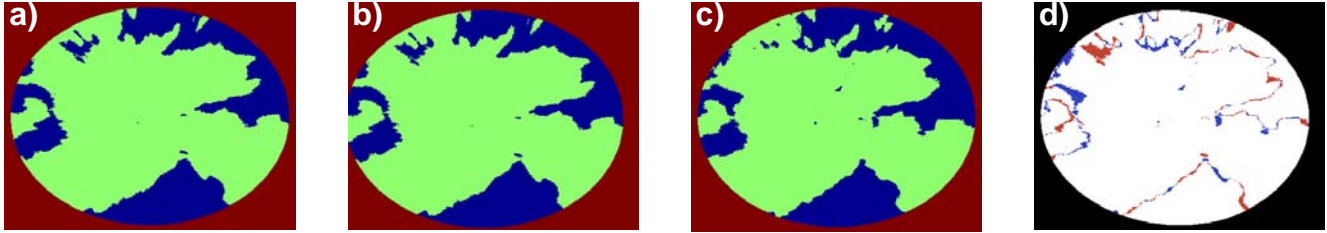


Figure 5: The forecast cloud map (b) is produced by advecting the cloud map at time t_0 (a) in the direction of the motion vector (here XX degrees). To determine the forecast error (d), the future cloud map at time $t_0 + 30$ seconds (c) is compared to the forecast (b). Blue and red colors in (d) show forecast errors (blue: pixel forecast cloudy and but actually clear; red: pixel forecast clear but actually cloudy) and white indicates accurate forecasts.

3. Results

3.1 Selection of Days

To assess the accuracy of sky imager forecasts, we selected relevant scenarios with typical sky conditions and high image quality. In our binary (cloud / no cloud) system, entirely clear or overcast days will always result in perfect forecast and these days are eliminated. Furthermore days with multiple cloud layers moving in different directions, rapid cloud deformation, formation, or evaporation were removed. Lastly the heating system on the imager failed for part of the year leading to excessive dirt aggregation on the mirror because of dew that made cloud detection impossible. Single layer broken clouds without rapid deformation moving across the sky are thought to be the best scenario to test the potential of the method. Sky condition occurrence frequency measured from a ceilometer at KNKX in 2010 (Table 1) provides context as to the fraction of time this method is useful in the present form. The following days were analyzed: September 14, 2009; October 4, 2009; March 4, 2010; and March 10, 2010.

Table 1 Sky condition occurrence frequency from a ceilometer at Miramar Naval Air Station (KNKX) in 2010. Partly cloudy conditions are defined as few, scattered, or broken clouds.

| Sky conditions | % Occurrence | Layers during Partly Cloudy | % Occurrence |
|----------------|--------------|-----------------------------|--------------|
| Clear sky | 18.2 | Multiple cloud layers | 34.8 |
| Overcast | 22.5 | Single cloud layer | 65.2 |
| Partly cloudy | 59.3 | | |

1

2 3.2 Cloud Decision

3 Since cloud decision images can only be validated visually, we describe here qualitative
 4 experiences of applying our method. In Fig. 6a, sky imager ZAs larger than 75° correspond to the
 5 horizon, and small sun-pixel-angles (approximately $< 35^\circ$) correspond to the circumsolar region,
 6 respectively. It can be seen in Fig. 6a that clear pixels away from the sun and horizon have rather
 7 uniform RBR. Decreasing the distance from sun and horizon increases RBR because the forward
 8 scattering of sunlight turns the horizon and the circumsolar region whiter and brighter.

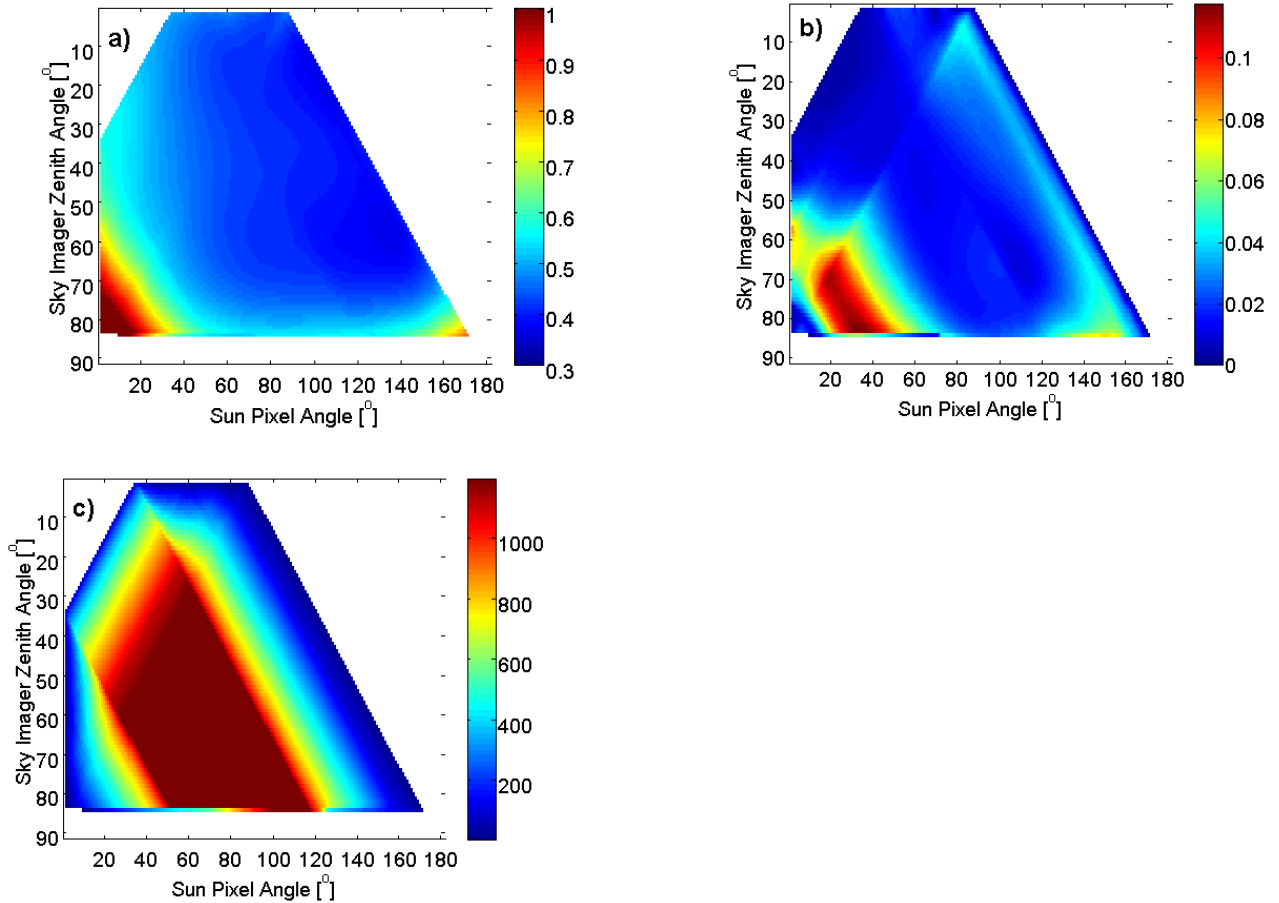


Figure 6: (a) Average RBR (colorbar) as a function of zenith angle and sun-pixel-angle based on TSI imagery on a clear day (September 24, 2009). This image is used to generate the clear sky library in Fig. 3b. (b) Standard deviation (colorbar) of clear sky RBR and (c) Number of occurrence (colorbar) for each zenith angle and sun-pixel-angle pair.

9

1 Figure 6b presents the standard deviation of the clear sky RBR to quantify the RBR variation during
2 the (clear) day in Fig. 6a. Larger variation of RBR leads to less accurate cloud decisions since it makes
3 it more likely that a clear sky RBR would be larger than the threshold and classified as cloudy. For sun-
4 pixel-angles greater than 50° and sky imager ZA less than 60° (i.e. in the region with the highest
5 occurrence, Fig. 6c) the variation in the clear sky RBR is small and our method performs well. However,
6 the standard deviation of the RBR in the circumsolar region is found to be largest when the sun is near
7 the horizon (low sun-pixel-angle and high zenith angle). Anecdotal observations confirm that clear
8 conditions in the circumsolar region at low sun elevation are often misclassified as cloudy while the
9 horizon and circumsolar region appear white. In addition, at larger solar ZAs less sunlight scattered by
10 clouds reaches the TSI due to shading by other clouds, increased optical path length through the
11 atmosphere, and near 90° scattering angles. These effects cause clouds to be dark in color at the
12 cloud-base and results in a smaller RBR than the CSL leading to incorrect clear classification.

13 Optically thin clouds are bluish because the background clear sky is visible through the cloud and
14 are notoriously difficult to detect automatically (Shields et al. 1998) as their RBR is only slightly larger
15 than the clear sky. If the RBR threshold is lowered to detect thin clouds it will increase false cloudy
16 (cloud detected but no cloud exists) detections, especially in the circumsolar region. For our application
17 of solar forecasting and sky imagers located in proximity to solar power plants, the CSL threshold is
18 optimized to provide a more accurate cloud decision in the circumsolar region at the expense of thin
19 cloud detection.

20 Optically thick clouds have smaller RBR than white clouds and bright regions. Optically thick clouds
21 can be detected accurately in regions with small CSL RBR (Fig. 6a). However, near the horizon or the
22 circumsolar region, thick clouds are often misclassified depending on the sun obscuration. If the sun is
23 unobscured (not shown), SP is large and dark clouds near the sun are misclassified as clear. When the
24 sun is obscured, dark clouds are correctly classified due to the SP algorithm (Fig. 7).

25

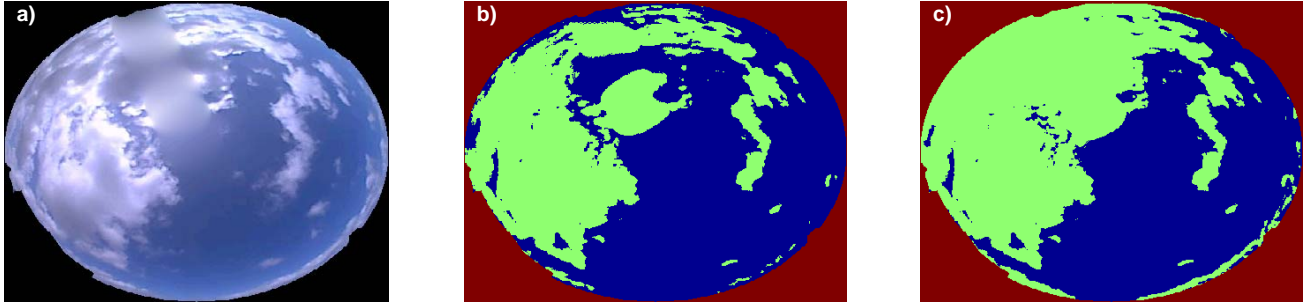


Figure 7: Cloud decision comparison between clear sky library (CSL) method (b) and integrated CSL and sunshine parameter method (c) on October 4, 2009 12:43:30 PST.

To summarize the errors: cloud decision when the sun is near the horizon is not reliable; false clouds appear on the horizon and in the circumsolar region; false clear conditions occur for dark clouds on the horizon and in the circumsolar region; and optically thin clouds are not detected. Cloud decision behind the shadow band and camera arm is expected to be unreliable since its RBR is interpolated from surrounding areas. Differing aerosol optical depth between the day when the CSL was generated and the day under consideration can degrade the accuracy of the cloud decision.

3.3 Cloud Motion

Figure 8 illustrates the computed motion vector field at several stages in the quality control process. A reduction in the CCC usually implies smaller accuracy of motion vectors. Reduced CCC can be the result of cloud formation, deformation, and evaporation. Also the appearance of a cloud may change over time due to different camera white balancing, lighting on the cloud, and different viewing geometries.

After removing vectors in the circumsolar and clear sky region, and vectors with CCCs less than 0.8, most remaining vectors are uniform (Fig. 8b). By computing the average and standard deviation of the vector field, the remaining outlier vectors are eliminated (Fig. 8c).

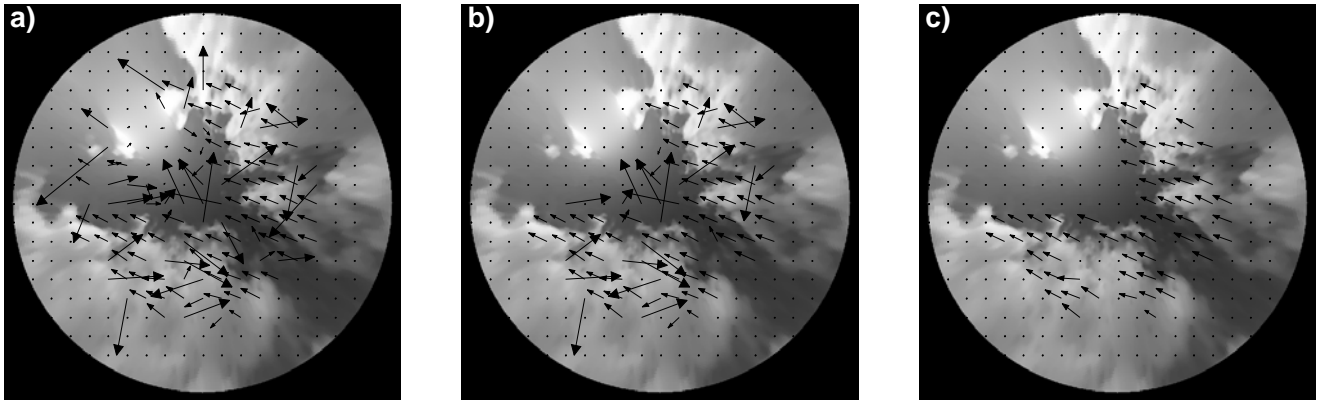


Figure 8: Illustration of procedures for obtaining a motion vector field on a sky image in sky coordinates on March 4, 10:21:30 PST. (a) Original vector field resulting from the cross-correlation method, (b) after removing vectors near the sun and vectors with a correlation of less than 0.8, and (c) after removing outliers. The average cloud velocity was 4.0 m s^{-1} .

1

2

3

4

5

6

7

8

9

10

Incorrect motion vectors are found primarily in overcast and nearly clear sky conditions (Fig. 9). In overcast skies, the sky contrast is reduced resulting in low CCC. In nearly clear sky conditions, clouds are often thin and evaporate. If the sky contains clouds with sharp cloud boundaries, CCM generally performs well. Due to the general persistence of cloud velocities (usually within 2 m s^{-1} over several minutes), erroneous decision vectors can be identified since they are associated with large cloud velocity fluctuations (Fig. 9a). If the cloud velocity changes by more than two standard deviations of velocity over the past 5 minutes, the current cloud velocity is replaced by the average velocity over the past 5 minutes.

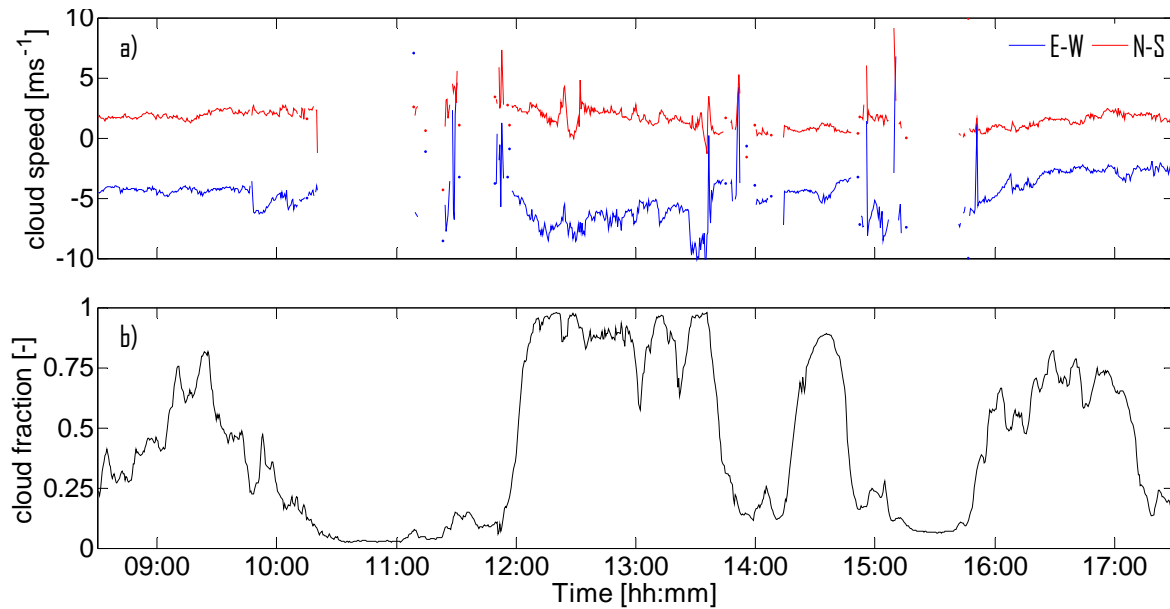


Figure 9: Time series plot of eastward and northward cloud velocities (a) and cloud fraction (b) on March 10, 2010. The velocities are persistent under partial cloud cover (0800-1030 PST and 1530-1730 PST), but fluctuate largely in overcast and almost clear sky conditions.

3.4 Nowcast of Binary Cloudy Conditions

Using the binary irradiance technique described in section 2.3, GHI time series were produced for the ground stations listed in Table 2 Location and **status information for w** with daily availability on the four days listed in section 3.1. The UCSD testbed had 6 meteorological stations monitoring global horizontal irradiance (GHI) at 1 Hz with Li-COR 200SZ pyranometers (Fig. 1). The instruments are spatially close enough that they can be calibrated against each other on clear days to ensure consistency (see Lave et al. 2011 for a more detailed study of the irradiance fluctuations at these sites). The 1 Hz GHI data collection is faster than the image capture frequency, so validation GHI time series were constructed for each station by using only the data points gathered at the time when the sky image was taken (no averaging is performed).

Table 2 Location and status information for weather stations used to validate TSI cloud shadow maps

| Station Identifier | RIMC | BMSB | EBU2 | TIOG | HUBB | MOCC |
|--------------------|-----------|-----------|-----------|-----------|-----------|-----------|
| | | | Location | | | |
| latitude [deg] | 32.8852 | 32.8758 | 32.8813 | 32.8790 | 32.8673 | 32.8782 |
| longitude [deg] | -117.2401 | -117.2362 | -117.2330 | -117.2434 | -117.2535 | -117.2231 |
| altitude [m] | 124 | 134 | 104 | 158 | 12 | 104 |

| | | | | | | |
|---------------------|--------------------|-----------------|-----|-------------------------------|-------|-------|
| distance to TSI [m] | 15 | 1,107 | 789 | 760 | 2,362 | 1,770 |
| | Operational Status | | | | | |
| Sept 14, 2009 | ■ | ■ | ■ | ■ | ■ | ■ |
| Oct 4, 2009 | ■ | ■ | ■ | N/A | N/A | ■ |
| Mar 4, 2010 | N/A | N/A | ■ | N/A | ■ | N/A |
| Mar 10, 2010 | ■ | N/A | ■ | N/A | ■ | N/A |
| | ■ Operational | N/A Unavailable | | ■ Cloud too low, out of range | | |

1 Figure 10, showing MOCC on October 4, indicates that GHI variability can be estimated using a TSI.

2 The morning period is dominated by false clouds due to MOCC's projected sky position being located in

3 the shadowband area of the circumsolar region. Once the projected sky position moved into the outer

4 region the TSI nowcasts the sky conditions between the sun and MOCC accurately, correctly predicting

5 the sky condition 68.3% in clear conditions and 80.4% in cloudy conditions, where clear is defined as a

6 clear sky index (*kt*) greater than 0.7.

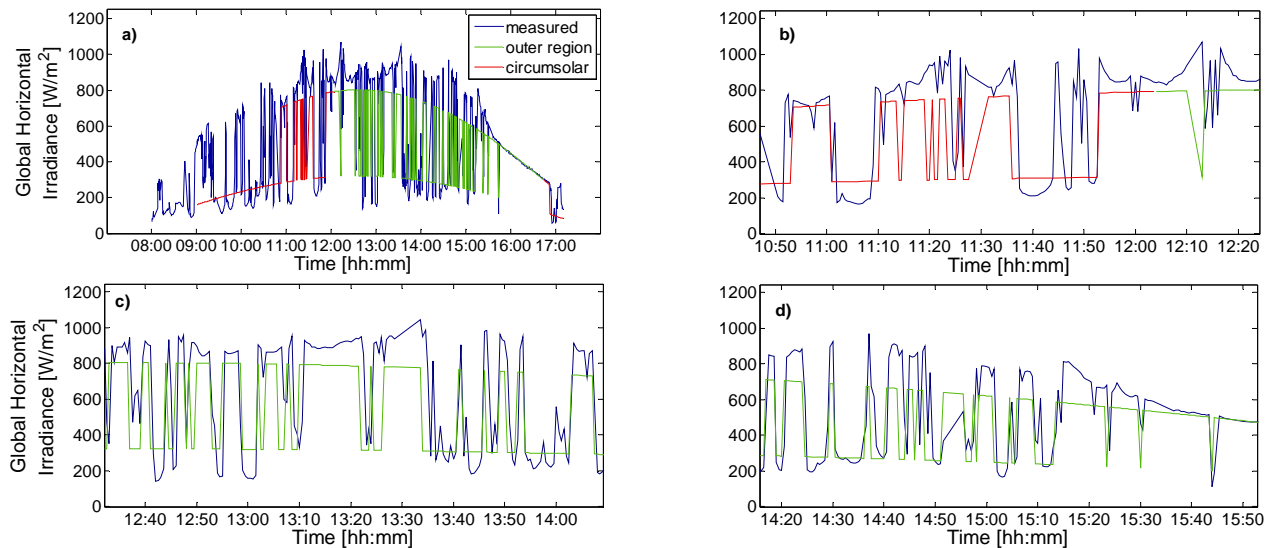


Figure 10: Time series (a) of MOCC station for October 4, 2009 showing measured GHI (blue) versus the TSI nowcast. The TSI shadow map is separated into circumsolar (red) and outer-region (green). Nowcasts of the TSI after 1100 PST (b),(c) and (d) match the trends in the measured data well.

7

8 Nowcast accuracy is expected to decrease with distance from the TSI due to the lower resolution at

9 large sky imager ZAs (in an extreme case on March 4, low clouds over the HUBB station 2.4 km to the

10 southwest were out of sight of the TSI). However, the TSI was able to capture the trends in GHI at the

1 HUBB station (Figure 11) on the other days. When HUBB was in the outer region, the TSI correctly
 2 predicted clear skies 60.0% of the time, and cloudy skies 90.6% of the time.

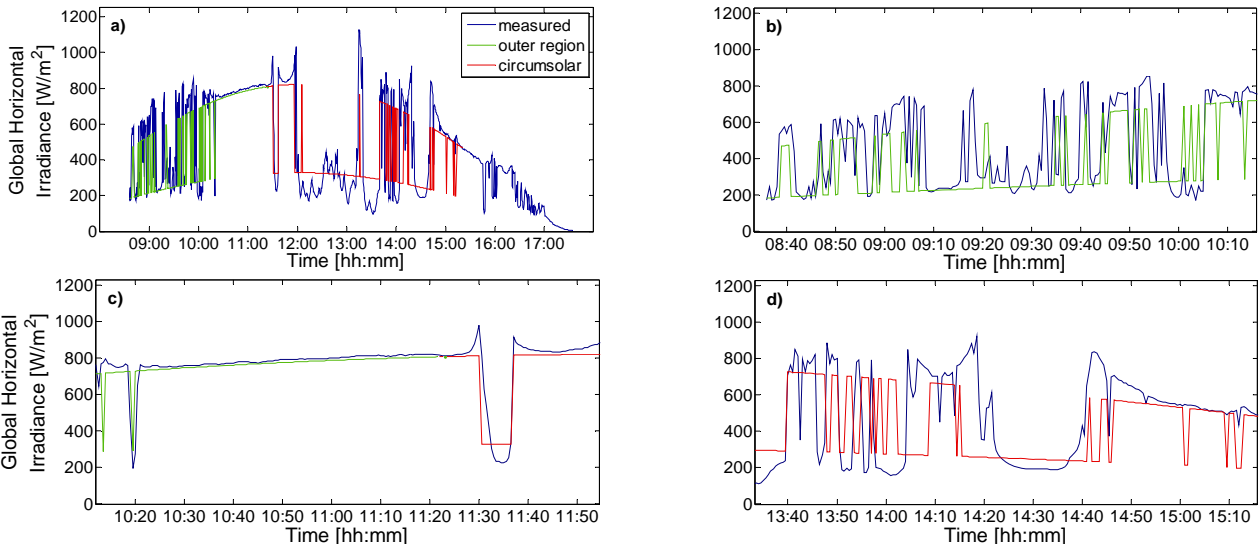


Figure 11: Time series (a) of HUBB station for March 10, 2010 showing measured GHI (blue) versus TSI nowcast, with the latter separated into circumsolar (red) and outer-region (green). Zooming in (b), (c) and (d) shows the ability of the TSI to produce nowcasts for a distant site.

3

4 Since binary descriptive statistics are most appropriate to validate the binary TSI cloud estimate the

5 clear-cloudy co-occurrence was tabulated (Table 3) for images taken when the cloud fraction was in the

6 range $0.2 \leq cf \leq 0.8$. Cloud fraction is defined as percent hemispheric cloud coverage weighted by

7 solid angle (as opposed to by pixel). This restriction on cloud fraction is used to ensure that the results

8 are not biased by nearly cloud free or overcast conditions which would result in a near perfect sky

9 condition nowcast. For the four days chosen and for all available stations (Table 2 Location and **status**

10 **information for w**), the TSI correctly estimated the condition of the sky 69.7% of the time in the outer

11 region. This ratio was significantly different in measured clear (59.4%) and cloudy conditions (81.5%). It

12 was more often predicted cloudy when it was clear than predicted clear when it was cloudy. A cause of

13 this asymmetry could be that the technique described in section 2.3 assumes that clouds have a

14 negligible vertical extent at a uniform height; when the side of a cloud is measured it increases the total

15 cloud coverage measured by TSI over the actual amount.

Table 3 Distribution of measured versus TSI nowcast clear (CLR) and cloudy (CLD) conditions for skies

with cloud fraction $0.2 \leq cf \leq 0.8$ (fraction of hemispheric solid angle). In line 1, the first term denotes measured clear sky index, and the second is the TSI estimate, thus CLD/CLR means the ground station measured cloudy conditions ($kt \leq 0.7$) but the TSI estimated clear. CLR_m and CLD_m are the number of clear and cloudy measurements, respectively, in the outer region. The last column shows the overall statistics (not conditioned on cloudy or clear). Data is for all stations.

| | CLR/CLR [%] | CLR/CLD [%] | CLR_m | CLD/CLR [%] | CLD/CLD [%] | CLD_m | % correct |
|---------------|----------------|----------------|---------|----------------|----------------|---------|--------------|
| Sept 14, 2009 | 47.1 | 52.9 | 594 | 28.3 | 71.7 | 368 | 56.6 |
| Oct 4, 2009 | 76.2 | 23.8 | 441 | 10.3 | 89.7 | 419 | 82.8 |
| Mar 4, 2010 | 63.1 | 36.9 | 157 | 33.3 | 66.7 | 144 | 64.8 |
| Mar 10, 2010 | 52.7 | 47.2 | 110 | 7.0 | 93.0 | 201 | 78.8 |
| Total | 59.4 | 40.6 | 1302 | 18.5 | 81.5 | 1132 | 69.7 |

1

2 The error metrics of the sky imager GHI estimates (Fig. 10, 11) indicate a negative bias (not shown).

3 The negative bias in the circumsolar region is primarily due to false clouds decreasing the estimated

4 GHI. In the outer region the negative bias is mostly caused by the cloudy bias noted above and cloud

5 enhancement effects whereby the solar disk is not obscured but forward scattering of radiation by

6 clouds located near the solar disk increases the diffuse radiation component and thus the overall GHI.

7 Since the TSI estimate assumes a clear sky index of unity when the sun is not obscured it

8 underestimates the clear sky GHI as well.

9 **3.5 Minutes Ahead Forecast**

10 The performance of a minutes ahead forecast is discussed in this section for four days following the

11 metrics established in section 2.5 and Fig. 5. Figure 12 show the time series of cloud speed, cloud

12 fraction, and errors for a 30 second forecast on September 14. Since both clear and overcast skies

13 always have perfect forecasts due to the use of binary cloud maps, cloud speeds and forecast errors

14 are not assigned for these times.

15

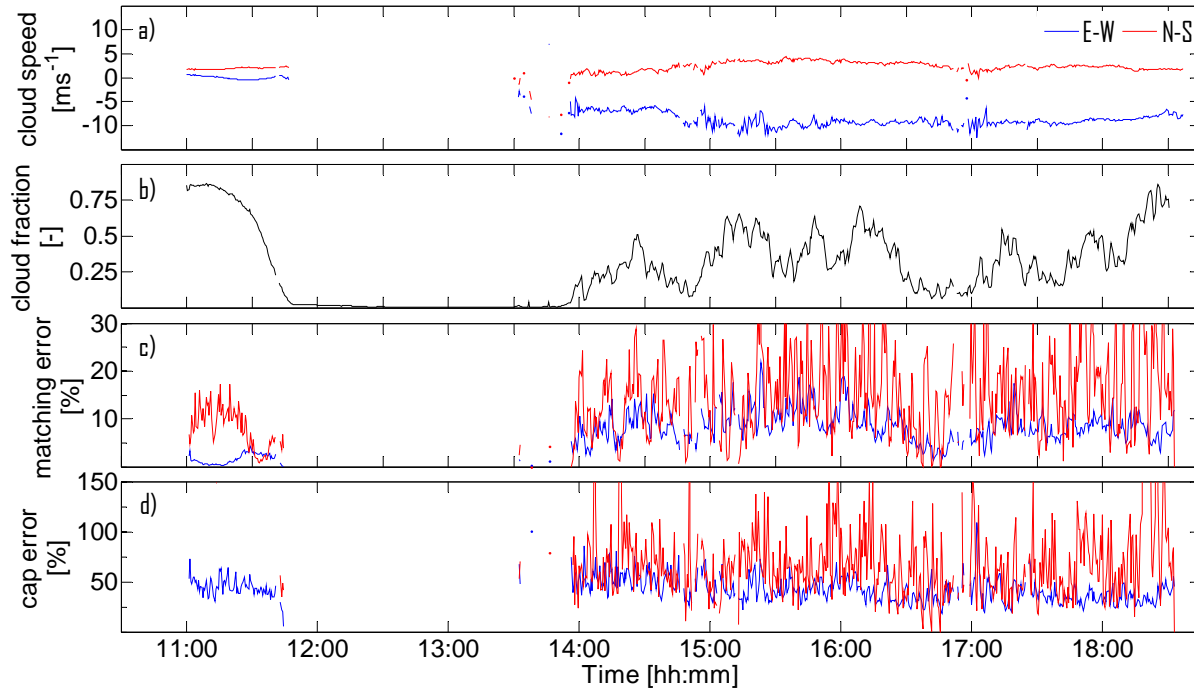


Figure 12: Time series of (a) westward and southward cloud speed, (b) cloud fraction, (c) matching error, and (d) cloud-advection-versus-persistence (cap) error obtained every 30 seconds on September 14, 2009. The red line in c) and d) indicates the error in the circumsolar region, while the blue line indicates the error in the outer region. In clear conditions (e.g. 1145 – 1350 PST) no cloud speed is determined and the errors are zero.

1 On September 14, 2009 a transition from overcast to clear sky occurred between 1100 PST and
2 1200 PST with clouds at an altitude of 610 m moving from north to south at less than 2 m s^{-1} . In the
3 afternoon, thin clouds moved at high speed eastward and were evaporating and deforming rapidly, as
4 evident by the variable cloud fraction. As a result, the matching error in the afternoon is much larger
5 than between 1100-1200 PST. Despite the poor matching error, September 14 has similar cap error as
6 the other days. The matching error is larger than on other days, but the large cloud speed causes large
7 persistence errors which reduces the cap error. The invariance of the cap error over time suggests that
8 the normalization by the persistence image provides a universal performance metric. While matching
9 errors become small when the cloud cover fraction is small or large (the edge-to-area ratio is small in
10 the latter case), the cap error is not sensitive to cloud cover fraction. The cap error is however sensitive
11 to cloud speed.

In the circumsolar region, the large errors are a result of the poor cloud decision. While the SP dramatically increases the accuracy of the cloud decision in the circumsolar region, its high variability occasionally causes cloud decision errors. Additionally, a false cloud detection results when two different clouds bordering the shadowband on both sides are interpolated across. Both issues cause a step change in the cloud decision in a large area between consecutive images which leads to erroneous forecasts.

Mean and standard deviation of outer region error metrics for a 30 second forecast are summarized in Table 4. The mean matching errors are 3 to 7% and the cap errors are 40 to 45%. The cap error of less than unity indicates that translating the cloud map improves the forecast compared with persistence. The mean matching error scales with cloud speed. Otherwise, the comparison of different days does not yield strong correlations between different variables, presumably due to intra-day variability.

Table 4 Mean and standard deviation of matching and cap error (Eq. 5 and 6) for the outer region on four different days. The errors are averaged only during conditions that were not clear or overcast. Since errors during overcast and clear conditions are zero, the errors in the table are biased high.

| | mean e_m [%] | mean e_{cap} [%] | std e_m [%] | std e_{cap} [%] | avg cloud fraction [-] | avg cloud speed [m s ⁻¹] | avg cloud height [m] |
|---------------|-------------------|-----------------------|------------------|----------------------|------------------------------|--|----------------------------|
| Sept 14, 2009 | 6.26 | 42.8 | 3.24 | 14.2 | 0.135 | 7.79 | 840 |
| Oct 4, 2009 | 4.09 | 40.0 | 1.48 | 7.45 | 0.473 | 3.75 | 1090 |
| Mar 4, 2010 | 3.16 | 44.7 | 1.33 | 10.5 | 0.276 | 2.95 | 610 |
| Mar 10, 2010 | 3.85 | 41.1 | 2.40 | 20.2 | 0.427 | 4.49 | 1220 |

Table 5 shows the mean total matching error and total cap error for a 30 seconds to 5 minutes ahead forecast. Mean forecast matching errors increase less than linearly from around 6% for 30 second forecasts to 23-30% for 5 minute forecasts. Mean cap errors are less than 80% out to 5 minutes, except on September 14, 2009 when large cloud speeds were observed. Note that while the outer region matching error was considered for 30 second forecasts, here the total (circumsolar and outer region) errors are considered as clouds are frequently advected between the circumsolar region and the outer region (depending upon cloud speed and direction).

Table 5 Mean total matching error and total cap error for a 30 second to 5 minute ahead forecast. The errors are averaged only during conditions that were not clear or overcast and when the entire scene had not been advected out of the field-of-view. Since errors during overcast and clear conditions are zero, the errors in the table are biased high.

| | 30 sec | 1 min | 2 min | 3 min | 4 min | 5 min | 30 sec | 1 min | 2 min | 3 min | 4 min | 5 min | Time until advection out of scene [min] |
|---------------|-----------|-------|-------|-------|-------|-------|---------------|-------|-------|-------|-------|-------|---|
| | e_m [%] | | | | | | e_{cap} [%] | | | | | | |
| Sept 14, 2009 | 8.67 | 13.5 | 20.1 | 23.8 | 27.2 | 28.0 | 45.0 | 51.5 | 63.9 | 70.0 | 76.5 | 123 | 4 - 27 |
| Oct 4, 2009 | 6.01 | 9.84 | 15.9 | 20.5 | 24.2 | 27.1 | 47.2 | 49.8 | 55.6 | 61.5 | 66.6 | 70.3 | 8 - 18 |
| Mar 4, 2010 | 5.36 | 8.68 | 13.6 | 17.3 | 20.4 | 23.4 | 54.6 | 55.3 | 59.3 | 63.4 | 67.7 | 71.8 | 9 - 24 |
| Mar 10, 2010 | 6.41 | 10.7 | 17.8 | 23.1 | 27.2 | 30.0 | 48.8 | 53.9 | 62.3 | 68.8 | 75.1 | 78.0 | 9 - 15 |

1

2

3

4

5

6

7

8

9

10

11

12

13

14

15

16

17

18

19

20

21

The errors can decrease in time (Fig. 13) if for example, a cloud that was forecast incorrectly is advected out of the scene while another cloud that was forecast correctly remains. The time until the initially measured cloud field is advected out of the scene determines maximum possible total sky imager forecast horizons for the area surrounding the imager. The footprint of the cloud shadows on the ground varies with sun angle and cloud height and the forecast horizon is a function of cloud height and cloud speed. For the low cloud heights and cloud speeds observed, the maximum forecast horizon was about 5 to 25 minutes. The following sources of forecast error are observed:

(i) In general, cloud deformation contributes most to forecast error. In our low latitude coastal areas with mostly mesoscale weather patterns, changing cloud patterns are more common than in more synoptically driven areas. Large solar irradiance can lead to short convection and cloud evaporation time scales. The rapid condensation and evaporation and associated deformation of clouds introduce complexity to deterministic cloud forecasting.

(ii) As discussed in section 3.4, perspective and occlusion effects on clouds are another source of error resulting from the two-dimensionality of the sky image. The sides of approaching clouds are interpreted as cloud bottoms. Consequently, as the clouds approach the sky imager, the perspective changes until only the cloud bottom is visible leading to a perceived decrease in cloud sizes and change in cloud shape. The perspective error may also create the illusion that there is one cloud while there are two nearby but separate cloud. Generally, the perspective error is inversely proportional to CBH; it will be largest for tall thunderstorm clouds and small for thin stratus clouds. A network of sky imagers with different perspectives could reduce this forecast error.

1 (iii) Heterogeneity of cloud velocity. Usually, the cloud velocity computed from cross-correlation is
 2 representative of the velocity of all clouds in the image. In rare cases, however, cumulus clouds to the
 3 east of the sky imager were moving at a different velocity than stratiform clouds to the west. Since our
 4 forecast assumes a homogeneous cloud velocity (roughly the size weighted average velocity of the two
 5 cloud layers), large forecast errors result.

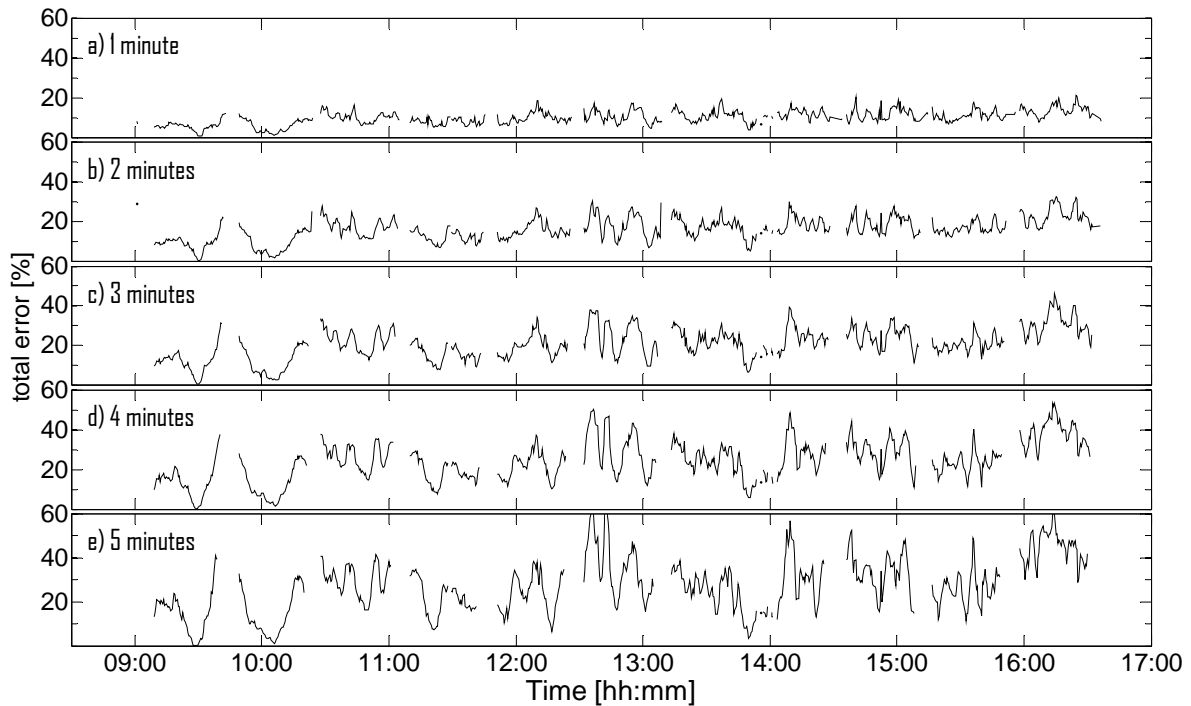


Figure 13: Total matching error for different forecast horizons on October 4, 2009. (a) 1 minute, (b) 2 minutes, (c) 3 minutes, (d) 4 minutes, (e) 5 minutes. Missing data occur because of missing images, clear or overcast skies, and when the entire scene had been advected out of the field-of-view.

6 4. Conclusions and Future Work

7 A technique for intra-hour, sub-kilometer cloud shadow nowcasting and forecasting using a ground-
 8 based sky imager was presented for selected days at the UC San Diego solar energy testbed. The use
 9 of sky imagery to assess the solar resource for solar energy applications shows much potential for
 10 augmenting the spatial and temporal resolution provided by satellite and numerical forecasting methods.
 11 Only short deterministic forecast horizons are feasible using a single TSI at our site due to low clouds

1 and large cloud variability at the fine spatial scale studied. Capturing these features deterministically is
2 nearly impossible with satellites or numerical weather prediction.

3 The method's accuracy is also limited by the shortcomings of the sky imager used. Part of the data
4 within each image is lost due to obscuration by the camera arm and shadowband. Low dynamic range
5 causes images to saturate easily near the sun, even with automatic gain control (AGC) of the CCD
6 camera. AGC causes its own problems because the output signal strength fluctuates between images,
7 leading to shifting intensity histograms and making spectral composition based cloud decisions less
8 reliable. Inaccuracies in the forecast sky conditions are also due to cloud deformation, evaporation, and
9 condensation, as well as uncertainty in cloud base height. The effect of these hardware limitations is
10 evident by the increased errors in the circumsolar region (Fig. 12).

11 Despite these shortcomings cloud shadows in the outer regions are correctly nowcast 70% of the
12 time. Cloud-advection-versus-persistence (cap) errors were found to be a universal metric to compare
13 forecast performance (Table 4, 5); for 30 second forecast, a 50-60% reduction in forecast error
14 compared to persistence was found. The error would be further reduced if it were spatially averaged
15 over a large solar array rather than computed on a pixel-by-pixel basis. Matching forecast errors
16 increase with cloud speed and forecast horizon.

17 Future work will include several elements to improve forecast accuracy. Replacing the TSI by a sky
18 imager that does not use a shadowband (Cazorla et al. 2008, 2009, Heinle et al. 2010) will increase the
19 usable fraction of the image. A CCD camera with large well-depth will be deployed to minimize
20 saturation in direct sunlight. A fisheye lens with an equisolid angle projection will improve the image
21 resolution at low elevation angles to increase forecast horizon and accuracy at long forecast horizons.
22 On-site cloud height will be retrieved using a ceilometer collocated with the sky imager to improve the
23 geometry-based irradiance nowcasting. The CSL will be generated using data from more than one day
24 and will incorporate a third dimension by using SZA, which will help account for airmass and other
25 diurnal effects. CSL thresholding based on daily aerosol optical thickness will improve the cloud
26 decision since the spectral composition of clear sky is affected by scattering due to aerosols. Additional

sky imagers will be installed at the UC San Diego energy testbed to increase the coverage area and forecast horizon. This will allow the vertical extent of clouds to be determined with a 3D-reconstruction of clouds using stereography. Sky imagers are also currently being installed at inland sites to study cloud conditions likely to be experienced by solar power plants. The methods developed here for sky imagery will be combined with satellite- and numerically-based forecasts to yield a comprehensive and more accurate forecast product with different forecast horizons, with the goal of meeting the needs of utility, grid, and power plant operators.

Acknowledgements

We acknowledge (i) funding from DOE High Solar PV Penetration grant 10DE-EE002055, (ii) assistance with installation and maintenance of the sky imaging facility by Tex Xelowski, David Purtell, Mildred Mcmilion from RIMAC Sports Facilities, (iii) support from John Ratcliffe and Robert Serocki.

References

- Benjamin, S., Brown, J., Olson, J., Wilczak, J., Banta, R., DiMego, G., Weng, F., 2010. Improvements in NOAA modeling and data assimilation to improve guidance for the renewable energy industry. American Meteorological Society Conf.
- Beaubien, M., Freedman, J., 2001. Comparison of Two Imager-based Methods for Determination of Winds Aloft. American Meteorological Society Conf.
- Cano D., Monget J., Aubuisson M., Guillard H., Regas N., Wald L., 1986. A method for the determination of global solar radiation from meteorological satellite data. *Solar Energy* 37, 31–39.
- Cazorla, A., Olmo, F., Alados-Arboledas, L., 2008. Development of a sky imager for cloud cover assessment. *J. Opt. Soc. Am. A* 25, 29–39.
- Cazorla, A., Shields, J., Karr, M., Olmo, F., Burden, A., Alados-Arboledas, L. 2009. Technical Note: Determination of aerosol optical properties by a calibrated sky imager, *Atmos. Chem. Phys.*, 9, 6417–6427.
- Feister U., Shields, J., 2005. Cloud and radiance measurements with the VIS/NIR Daylight Whole Sky Imager at Lindenberg (Germany). *Meteorol. Z.*, 14, 627-639.
- Hamill, T., Nehrkorn, T., 1993. A short-term cloud forecast scheme using cross correlation. *Wea. Forecasting* 8, 401–411

1 Heinle, A., Macke, A., Srivastav, A., 2010. Automatic cloud classification of whole sky images. *Atmos.*
2 *Meas. Tech.*, 3, 557–567.

3

4 Huo, J., Lu, D., 2009. Cloud determination of all-sky images under low visibility conditions. *J. Atmosph.*
5 *Oceanic Technology* 26 (10), 2172–218.

6

7 Huo, J., Lu, D., 2010. Preliminary retrieval of aerosol optical depth from allsky images. *Adv. Atmos. Sci.*
8 27 (2), 421–426.

9

10 Ineichen, P., Perez R., 2002. A new airmass independent formulation for the Linke turbidity coefficient.
11 *Solar Energy*, 73(3), 151–157.

12

13 Ineichen, P., 2006. Comparison of eight clear sky broadband models against 16 independent data
14 banks. *Solar Energy* 80, 468– 478.

15

16 Johnson, R., Hering W., Shields, J., 1989. Automated visibility and cloud cover measurements with a
17 solid-state imaging system. Tech. Rep., University of California, San Diego, Scripps Institution of
18 Oceanography, Marine Physical Laboratory, SIO Ref. 89-7, GL-TR-89-0061, 128 pp.

19

20 Johnson, R., Shields, J., Koehler, T., 1991. Analysis and Interpretation of Simultaneous Multi-Station
21 Whole Sky Imagery. Marine Physical Laboratory, Scripps Institution of Oceanography, University of
22 California San Diego, SIO 91-3, PL-TR-91-2214

23

24 Kalisch, J., Macke, A., 2008. Estimation of the total cloud cover with high temporal resolution and
25 parameterization of short-term fluctuations of sea surface insolation. *Meteorol. Z.*, 17, 603-611.

26

27 Kassianov, E., Long, C., Christy, J., 2005. Cloud-base-height estimation from paired ground-based
28 hemispherical observations. *J. Appl. Meteor.*, 44, 1221–1233.

29

30 Lara-Fanego, V., Ruiz-Arias, JA., Pozo-Vazquez, D., Santos-Alamillos, F., Tovar-Pescador, J., 2011.
31 Evaluation of the WRF model solar irradiance forecasts in Andalusia (southern Spain).
32 doi:10.1016/j.solener.2011.02.014, *Solar Energy*.

33

34 Lave, M., Kleissl, J., Arias-Castro, A., 2011. High-frequency irradiance fluctuations and geographic
35 smoothing. Submitted to *Solar Energy*.

36

37 Linke, F., 1922. Transmissions-Koeffizient und Trübungsfaktor. *Beitr. Phys. fr. Atmos.* 10, 91–103.

38

39 Long, C. J., Sabburg, J., Calbó, J., Pagès, D., 2006. Retrieving cloud characteristics from ground-
40 based daytime color all-sky images. *J. Atmos. Ocean. Technol.* 23, 633–652.

41

42 Lorenz, E., Remund, J., Müller, S., Traunmüller, W., Steinmaurer, G., Pozo, D., Ruiz-Arias, J., Fanego,
43 V., Ramirez, L., Romeo, M., Kurz, C., Pomares, L., Guerrero, C., 2009. Benchmarking of different
44 approaches to forecast solar irradiance. 24th European Photovoltaic Solar Energy Conference,
45 Hamburg, Germany, 21.-25.

46

47 Mathiesen, P., Kleissl, J., 2011. Evaluation of numerical weather prediction for intra-day solar
48 forecasting in the CONUS. Submitted to *Solar Energy*.

49

50 Martins, F., Pereira, E., Abreu, S., 2007. Satellite-derived solar resource maps for Brazil under SWERA
51 project, *Solar Energy*, 81, 517-528, ISSN 0038-092X, DOI: 10.1016/j.solener.2006.07.009.

- 1
- 2 McCartney, E., 1976. Optics of the Atmosphere: Scattering by Molecules and Particles. John Wiley &
- 3 Sons, pp. 216.
- 4
- 5 Pereira, E., Martins, F., Abreu, S., Couto, P., Stuhlmann, R., Colle, S., 2000. Effects of burning of
- 6 biomass on satellite estimations of solar irradiation in Brazil, *Solar Energy*, 68, 91-107, ISSN 0038-
- 7 092X, DOI: 10.1016/S0038-092X(99)00044-4.
- 8
- 9 Perez, R., Ineichen, P., Moore, K., Kmiecik, M., Chain, C., George, R., Vignola, F., 2002. A new
- 10 operational model for satellite-derived irradiances: description and validation. *Solar Energy* 73, 307-
- 11 317.
- 12
- 13 Perez, R., Kivalov, S., Schlemmer, J., Hemker Jr., K., Renné, D., Hoff, T., 2010. Validation of short and
- 14 medium term operational solar radiation forecasts in the US. *Solar Energy* 84, 2161-2172.
- 15
- 16 Pfister, G., McKenzie, R., Liley, J., and Thomas. A., 2003. Cloud coverage based on all-sky imaging
- 17 and its impact on surface solar irradiance, *Journal of Applied Meteorology.*, 42, 1421–1434.
- 18
- 19 Remund, J., Perez, R., Lorenz, E., 2008. Comparison of Solar Radiation Forecasts for the USA. Proc.
- 20 of the 23rd European PV Conference, 1.9-4.9, Valencia, Spain.
- 21
- 22 Rigollier, C., Lefèvre, M., Wald, L., 2004. The method Heliosat-2 for deriving shortwave solar radiation
- 23 from satellite images, *Solar Energy*, 77, 159-169, ISSN 0038-092X, DOI:
- 24 10.1016/j.solener.2004.04.017.
- 25
- 26 Schmetz, J., 1989. Towards a surface radiation climatology: retrieval of downward irradiances from
- 27 satellites. *Atmos. Res.* 23, 287–321.
- 28
- 29 Schroedter-Homscheidt, M., Hoyer-Klick, C., Rikos, E., Tselepis, S., Pulvermüller, B., 2009.
- 30 Nowcasting and forecasting of solar irradiance for energy electricity generation, *SolarPACES Conf.*
- 31
- 32 Seiz, G., Shields, J., Feister, U., Baltsavias, E., Gruen, A., 2007. Cloud mapping with ground-based
- 33 photogrammetric cameras. *International Journal of Remote Sensing* 28 (9) 2001–2032.
- 34
- 35 Shields, J., Karr, M., Tooman, T., Sowle, D., Moore, S., 1998. The whole sky imager—a year of
- 36 progress. presented at the Eighth Atmospheric Radiation Measurement (ARM) Science Team
- 37 Meeting, Tucson, Arizona, March 23–27.
- 38
- 39 Shields, J., Johnson, R., Karr, M., Wertz, J., 1998. Automated Day/Night Whole Sky Imagers for Field
- 40 Assessment of Cloud Cover Distributions and Radiance Distributions. Tenth Symposium on
- 41 Meteorological Observations and Instrumentation, American Meteorological Society, pp165 – 170.
- 42
- 43 Shields, J., Karr, M., Burden, A., Johnson, R., Hodgkiss, W., 2007. Continuing Support of Cloud Free
- 44 Line of Sight Determination including Whole Sky Imaging of Clouds, Final Report for ONR Contract
- 45 N00014-01-D-0043 DO #13, Marine Physical Laboratory, Scripps Institution of Oceanography,
- 46 University of California San Diego, Technical Note 273.
- 47
- 48 Shields, J., Karr, M., Burden, A., Johnson, R., Mikuls, V., Streeter, J., Hodgkiss, W., 2009. Research
- 49 toward Multi-Site Characterization of Sky Obscuration by Clouds, Final Report for Grant N00244-
- 50 07-1-009, Marine Physical Laboratory, Scripps Institution of Oceanography, University of California
- 51 San Diego, Technical Note 274.

- 1
- 2 Zelenka, A., Perez, R., Seals, R., Renné, D., 1999. Effective accuracy of satellite-derived
- 3 irradiance. *Theor. Appl. Climatol.* 62, 199–207.